Journal of
Materials Chemistry A
Materials for energy and sustainability

Accepted Manuscript

This article can be cited before page numbers have been issued, to do this please use: Y. Qiao, J. Jian, H. Tang, S. Ji, Y. Liu, H. Liu, Y. Li, X. Li, F. Han, Z. Liu, T. Cui, G. Gou, L. Jiang, Y. Yang, B. Zhou, T. Ren and J. Zhou, *J. Mater. Chem. A*, 2022, DOI: 10.1039/D1TA09813F.

View Article Online
DOI: 10.1039/D1TA09813F

PAPER

Intelligent Nanomesh-Reinforced Graphene Pressure Sensor with Ultra Large Linear Range

Received 00th January 20xx,
Accepted 00th January 20xx

DOI: 10.1039/x0xx00000x

Yancong Qiao*[a], Jinming Jian[b], Hao Tang[a], Shourui Ji[b], Ying Liu[a], Haidong Liu[a], Yuanfang Li[a], Xiaoshi Li[b], Fei Han[c], Zhiyuan Liu[c], Tianrui Cui[b], Guangyang Gou[b], Lelun Jiang[a], Yi Yang[b], Bingpu Zhou[d], Tian-Ling Ren*[b], and Jianhua Zhou*[a]

Pressure sensor is an important device in daily life, especially for the physiological signal monitoring. However, to realize the intelligent pressure sensor, more features should be achieved, such as high sensitivity, large linearity range, in-situ signal processing, and automatic analysis. In this article, inspired by the reinforced concrete structure, the nanomesh-reinforced graphene pressure sensor (NRGPS) has been designed and realized with not only excellent mechanical performance but also water vapor permeability. Unlike the negative-resistance pressure sensor, the resistance of NRGPS increases under the larger pressure, which greatly increase the measuring range. With the nanomesh skeleton, the NRGPS has ultra large linearity (1 MPa), high sensitivity (4.19 kPa^{-1}), excellent stability (more than 10000 cycles). To explain the sensing mechanism of NRGPS, a finite element model was proposed from the microstructure of nanomesh-reinforced graphene. With the aids of large linearity and high sensitivity, the NRGPS can simulate the mechanical MOSFET and realize the in-situ pulse signal amplification. Finally, an intelligent tactile sensor was achieved by combining NRGPS with convolutional neural network. Convex braille number can be distinguished by the intelligent tactile sensor with an accuracy of 88%. This work has potential in the intelligent diagnosis and tactile reconstruction field.

Introduction

Due to the urgent need in various field, pressure sensors fabricated with many novel materials have been attracted much attention.[1, 2] Among these applications, the health monitoring is an important function of pressure sensor.[3-5] Human body is full of physiological signals, which can reflect the conditions of ourselves. Some signals have been widely used in the diagnosis and prevention of diseases not only in hospital, but also in our daily life. For example, the pulse wave has been widely used for the diagnosis in the traditional Chinese medicine.[6] The tactile signals can be applied to reconstruct the sensing function of disables.

To realized intelligent pressure sensor, much effort has been given. However, many features of pressure sensor should be further optimized, such as sensitivity, linearity range, comfortability, and stability. Traditional pressure sensor has the negative-resistance response.[7-10] With the increasing of pressure, the resistance would decrease. Therefore, the max variation of resistance can only be up to 100%. In addition, the sensitivity of pressure sensor would become smaller and saturated under larger pressure, which limits the application of device. To achieve the high-performance pressure sensor, many novel materials with good property have been used, such as graphene,[7, 8] nanowires,[11, 12] nanomesh,[13] etc. But these nanomaterials are trend to be broken under the high pressure, which limits the work range and linearity of the pressure sensor. For example, Wu et al. realized a large-range pressure sensor by graphene with a linearity range of 200 kPa.[14] However, the high pressure would greatly increase the size and density of cracks in the graphene. Therefore, the sensor would become unstable when the pressure larger than 200 kPa. Lee et al. demonstrated a pressure sensor based on Au, polyurethane

a. School of Biomedical Engineering, Sun Yat-Sen University, Shenzhen, 518707, China.
b. School of Integrated Circuits (SIC) and Beijing National Research Center for Information Science and Technology (BNRist), Tsinghua University, Beijing, 100084, China.
c. CAS Key Laboratory of Human-Machine Intelligence-Synergy Systems, Shenzhen Institutes of Advanced Technology, Chinese Academy of Sciences (CAS), Shenzhen 518055, China
d. Joint Key Laboratory of the Ministry of Education, Institute of Applied Physics and Materials Engineering, University of Macau, Avenida da Universidade, Taipa, Macau 999078, China.
*Email address: zhoujh33@mail.sysu.edu.cn; rentl@tsinghua.edu.cn; qiaoyc3@mail.sysu.edu.cn

Electronic Supplementary Information (ESI) available: [details of any supplementary information available should be included here]. See DOI: 10.1039/x0xx00000x

(PU), and polyvinyl alcohol (PVA) nanomesh, which has good comfortability.[13] Due to the lack of piezoresistive effect and small thickness, the work range of the Au nanomesh pressure sensor is 100 kPa with the sensitivity about 1 kPa^{-1} at 100 kPa. In addition, Au nanomesh was fabricated by the sputtering process, in which the Au only cover the surface of PU nanomesh. Also, tactile sensor, as one important type of pressure sensor, has shown promising applications in wearable electronics, artificial limb, and intelligent robot. Current tactile sensors are mainly focused on materials,[15-18] structure,[19-22] self-power,[23-25] and integrated array.[15, 26-28] However, to realize the intelligent pressure sensor, the algorithm is also indispensable. Sundaram et al. fabricated a scalable tactile glove covering the full hand with 548 pressure sensors based on commercial force-sensitive film patterned by the laser cutting, and the cost of glove is about US$10.[29] The stress distribution map was input into the convolutional neural network (CNN), and transfer learning method (ResNet-18) was used to identify objects. In addition, the database is importance to the algorithm. The sensor with high water permeability and comfort would lead to more user, which can help to enlarge the size of database. Inspired by the common-used reinforced concrete structure, whose mechanical property can greatly improve the compressive strength of concrete,[30-34] we herein propose and fabricate a nanomesh-reinforced graphene pressure sensor (NRGPS) based on PU nanomesh and laser scribed graphene (LSG). The PU nanomesh can be regarded as the skeleton of reduced graphene, which is similar to steel bar in the reinforced concrete. Besides, the laser scribing process make the

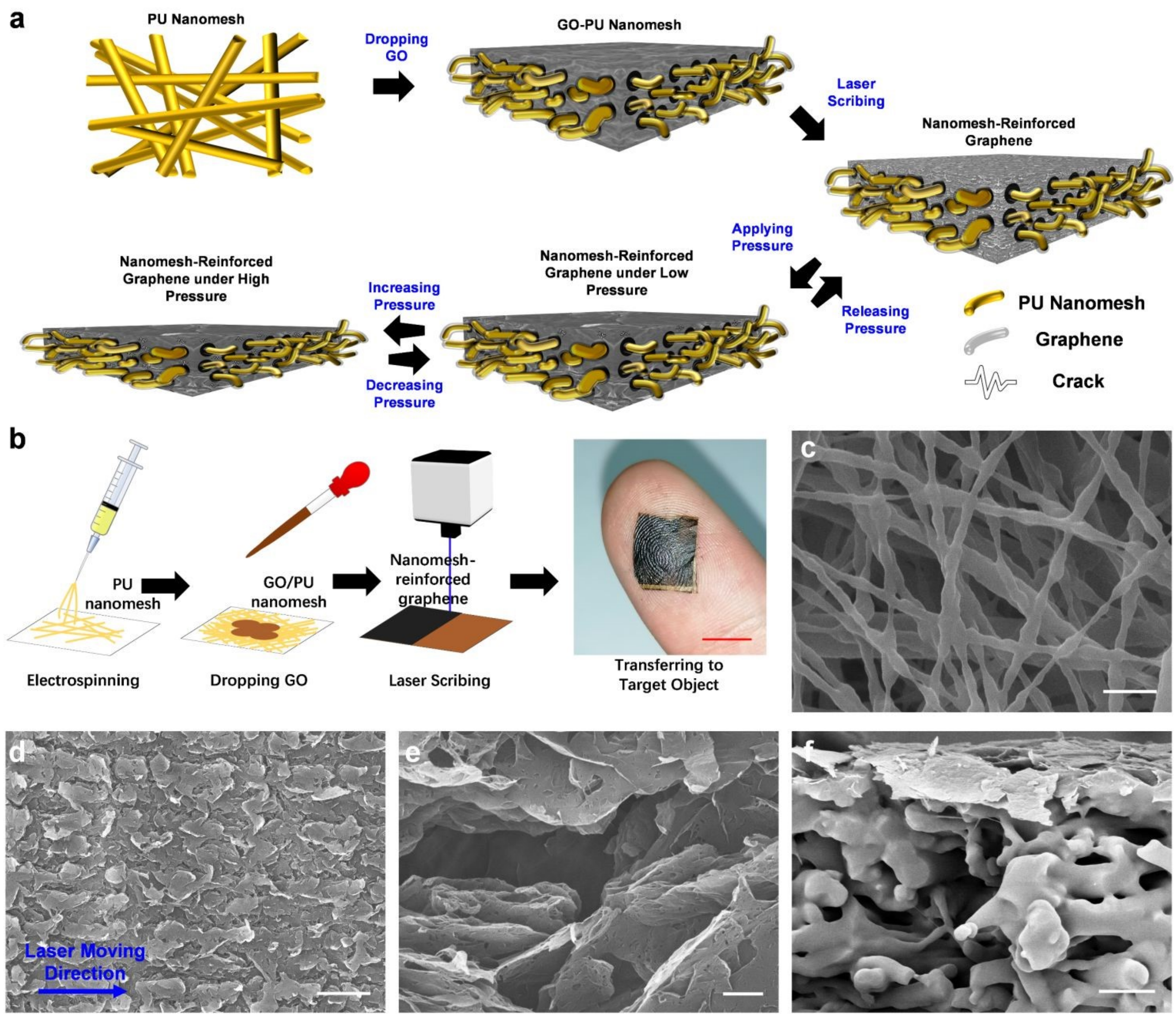

Figure 1. Design, preparation, and characteristics of the nanomesh-reinforced graphene. (a) Schematic diagram showing the fabrication of the PU nanomesh, GO-PU nanomesh, nanomesh-reinforced graphene in normal state, and the nanomesh-reinforced graphene in compressed state. (b) Schematic diagram of the fabrication process of the nanomesh-reinforced graphene, which including electrospinning PU nanomesh, dropping GO dispersion, laser scribing, and transferring the nanomesh-reinforced graphene to target object. The scale bar represents 1 cm. (c) The SEM image of the PU nanomesh fabricated by electrospinning. The scale bar represents 2 μm. (d) The SEM image of the LSG after the laser scribing on the PU nanomesh. The arrow represents the moving direction of the laser. The scale bar represents 200 μm. (e) The zoom in SEM image of the layer-structure LSG. The scale bar represents 5 μm. (f) The cross-section SEM image of the nanomesh-reinforced graphene. The scale bar represents 5 μm.

View Article Online
DOI: 10.1039/D1TA09813F

formation of the graphene coat around the superficial PU nanomesh tightly, rather than just cover the surface. Based on the nanomesh-reinforced structure, the size and density of cracks in graphene was limited, and the work range of our NRGPS can be up to 1 MPa, which is 5 times of graphene pressure sensor without nanomesh and 10 times of Au nanomesh pressure sensor. The nanomesh plays the role of skeleton, which greatly enlarges the linearity range of NRGPS and makes NRGPS more stable (Figure 1a). After more than 10000 compressing and releasing cycles, the NRGPS can still work well. The NRGPS has the positive-resistance response. With the increasing of pressure, the resistance would increase, which improves the sensitivity of the NRGPS. Based on the good piezoresistive effect of LSG, the sensitivity of NRGPS can be 4.19 kPa^{-1}. In addition, due to the porous structure of LSG and nanomesh, the nanomesh-reinforced graphene has good water vapor permeability, which almost as same as no obstruction. Similar porous graphene structure with good gas permeability can be used in CO_2 reduction with high efficiency[35, 36]. According to the microstructure of nanomesh-reinforced graphene, a finite element model was proposed to explain the working mechanism of the NRGPS, which fits the experimental result well. Besides, the intelligence of NRGPS can be illustrated in two aspects. First, it can process and respond to external stimuli. The NRGPS can be regarded as an intelligent hardware, which can realize the function of mechanical Metal Oxide Semiconductor Field Effect Transistor (MOSFET). By changing the quiescent pressure of NRGPS, the tactile signals can be amplified in situ rather than by circuit and software, and the amplification can be controlled. Second, combined with the CNN, the NRGPS can be used as intelligent tactile sensor. The convex braille number can be distinguished by only one NRGPS with an accuracy of 88%. It is worth mentioning that, the cost of single nanomesh-reinforced graphene is only about US$0.1, only about 1/20 of the Au nanomesh fabricated by sputtering,[37, 38] and 1/100 of the tactile glove mentioned above.[29]

Results and discussion

Design and Preparation of Nanomesh-reinforced Graphene

The fabrication process of nanomesh-reinforced graphene was shown in the Figure 1b. The PU nanomesh was firstly prepared by the electrospinning. 10 g PU pellets (Sigma-Aldrich) was mixed with 45 mL N,N-dimethylformamide (Aladdin). Then, the mixture was stirred for 3 h under 80 ℃. The PU solution was pumped in the speed of 0.8 mL/h, and 15 kV voltage was applied to the syringe needle. As shown in the Figure 1c, the diameter of the PU nanomesh is a few hundred nanometers to micrometers. In addition, much space exists inside the nanomesh. Therefore, the PU Nanomesh is a breathable structure. To grow the graphene in the PU nanomesh, the LSG technique was chosen. Compared with the common-used chemical vapor deposition, the LSG is a relatively low-temperature technique. In addition, the fast and local high temperature would not only do not destroy the nanomesh, but also coat the nanomesh by the reduced graphene. Before the LSG process, the GO dispersion (2 mg•mL^{-1} provided by XFNANO Materials Tech Co. Ltd.) was mixed with the tetrahydrofuran in a 5:1 volume ratio. Then, the dispersion was dropped onto the PU nanomesh. After the overnight evaporation, GO film was formed on the PU nanomesh to realize the GO/PU nanomesh (Figure S1). Thereafter, the GO/PU nanomesh was put into the homemade laser platform. The scribed GO area was reduced and converted into LSG (wavelength = 405 nm, power density = 20 mW/cm^2), and the GO/PU nanomesh was converted into the nanomesh-reinforced graphene. Because the laser moved in one direction, the LSG was composed of many parallel graphene strips. The width of strips is about 100 μm, which is close to the diameter of laser spot (Figure 1d). During the scribing process, many oxygen-containing functional groups in GO was eliminated and gas was released[39], which makes expansion of LSG and the porous structure inside the graphene flakes (Figure 1e). In addition, during the laser reduced process, the PU Nanomesh was immersed into the expanded LSG. The porous LSG and PU nanomesh structure makes the high gas permeability of nanomesh-reinforced graphene. The cross-section of nanomesh-reinforced graphene shows that the superficial nanomesh was covered and coated with graphene (Figure 1f and S2). The thickness of the nanomesh-reinforced graphene is 23 μm with the STD of 4.65 μm (Figure S3). In addition, the confocal microscope was also used to confirm the periodic fluctuation of nanomesh-reinforced

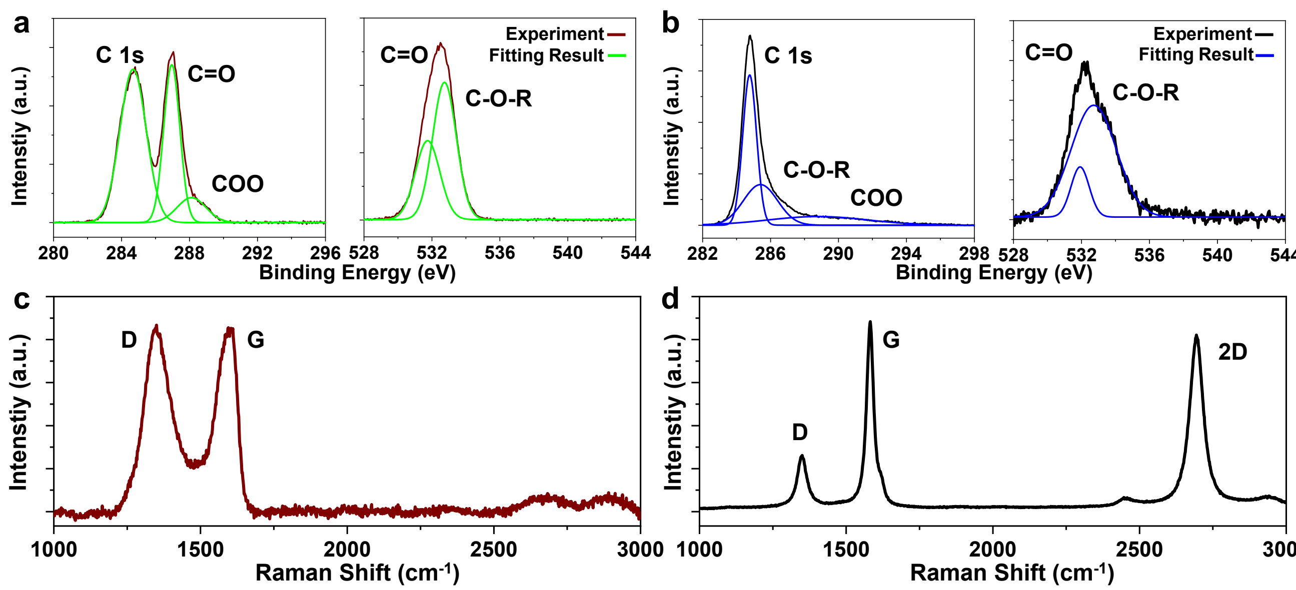

Figure 2. Characteristics of the nanomesh-reinforced graphene. (a) XPS measurements of the C 1s and O 1s in GO. The brown line corresponds to the experimental result, and the green line corresponds to the fitting result. (b) XPS measurements of the C 1s and O 1s in LSG. The black line corresponds to the experimental result, and the blue line corresponds to the fitting result. (c) The Raman shift of the GO coated on PU nanomesh. (d) The Raman shift of the LSG on PU nanomesh.

graphene (Figure S4 and S5). The fluctuation of nanomesh-reinforced graphene is more than 30 μm.

The X-ray photoelectron spectroscopy (XPS) was applied to confirm the laser induced reduction process of GO. The C/O atomic ratio of GO is 2.11. The C=O (287.0 eV of C 1s and 531.7 eV of O 1s), COO- (288.1 eV of C 1s), and C-O-R (532.7 eV of O 1s) were found in the C 1s and O 1s XPS of GO (Figure 2a). After the laser scribing, the C/O atomic ratio fast increased to 13.32. Therefore, many oxygen-containing functional groups disappeared. In addition, the loss of various oxygen-containing functional groups was also charactered by the XPS peak of the LSG. The relative peak heights between the C=O (531.9 eV of O 1s), COO- (288.8 eV of C 1s), and C-O-R (285.4 eV of C 1s and 532.7 eV of O 1s) to C 1s greatly decreased (Figure 2b). Raman shift was also used to prove the high quality of the LSG. As illustrated in the Figure 2c, the D and G peak has almost the same height (I_D/I_G = 1.01), and the 2D peak can also be ignored in the Raman shift of GO. After the laser scribing, 2D peak appear, and the relative height between G and D peak decreased greatly (I_D/I_G = 0.26), which is much lower than GO (Figure 2d). In addition, the full width at half maximum (FWHM) of the LSG is much smaller than the GO. Compared with amorphous carbon,[40, 41] the LSG has higher crystal quality.

To verify the water vapor permeability of nanomesh-reinforced graphene, four glass bottles were filled with 5 mL water, respectively. The first bottle was sealed using the cap. The second bottle was opened without any other treatment. The third bottle was sealed using the PU nanomesh. The PU nanomesh was firstly wetted by the atomized water droplets. Then, the nanomesh was put on the bottleneck. After dried by the hairy drier, the nanomesh can seal the bottleneck tightly. The fourth bottle was sealed with nanomesh-reinforced graphene by the same process as the PU nanomesh (Figure 3a). Thereafter, four kinds of bottles were placed at the same environment for 16 days (Temperature: 21 ℃, Humidity : 60.3%, Wind speed: 0 m/s, Atmospheric pressure: 1.0044×105 Pa, Altitude: 75 m). The weight loss of four bottles were 0.0313±0.0726 g, 1.2504± 0.0245 g, 1.0563±0.018g, and 1.0224±0.0391 g, corresponding to the water vapor transmission rate (WVTR) of 20.6 g×d^{-1}×m^{-2}, 822.76 g× d^{-1}×m^{-2}, 695.04 g×d^{-1}×m^{-2}, and 672.73 g×d^{-1}×m^{-2}, respectively. This result demonstrated the good water vapor permeability of nanomesh-reinforced graphene, which was almost as same as the open without any obstruction.

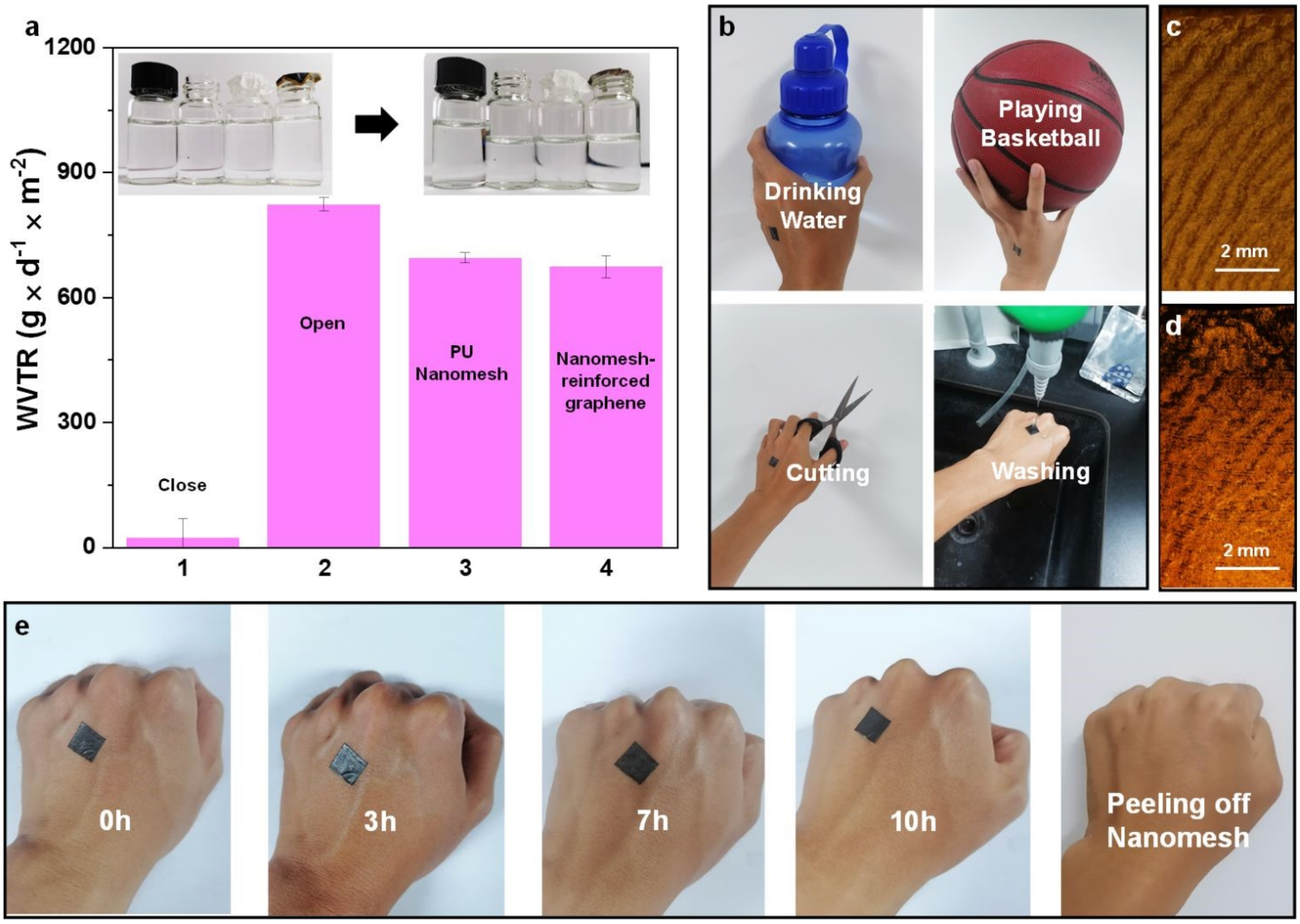

Figure 3. Water vapor permeability, stability, and skin compatibility of nanomesh-reinforced graphene. (a) The water volatilized conditions of four bottles with different sealing conditions. Each error bar was extracted from four samples. (b) The nanomesh-reinforced graphene attached on the hand of a tester, when the tester was drinking water, playing basketball, holding scissors, and washing hand. (c) The OCT picture of the tester's finger. The scale bar represents 2 mm. (d) The OCT picture of the tester's finger covered by the nanomesh-reinforced graphene. The scale bar represents 2 mm. (e) The nanomesh-reinforced graphene attached on the hand after transferred for 0h, 3h, 7h and 10h. After peeling off the nanomesh-reinforced graphene, the skin has no adverse feeling.

View Article Online
DOI: 10.1039/D1TA09813F

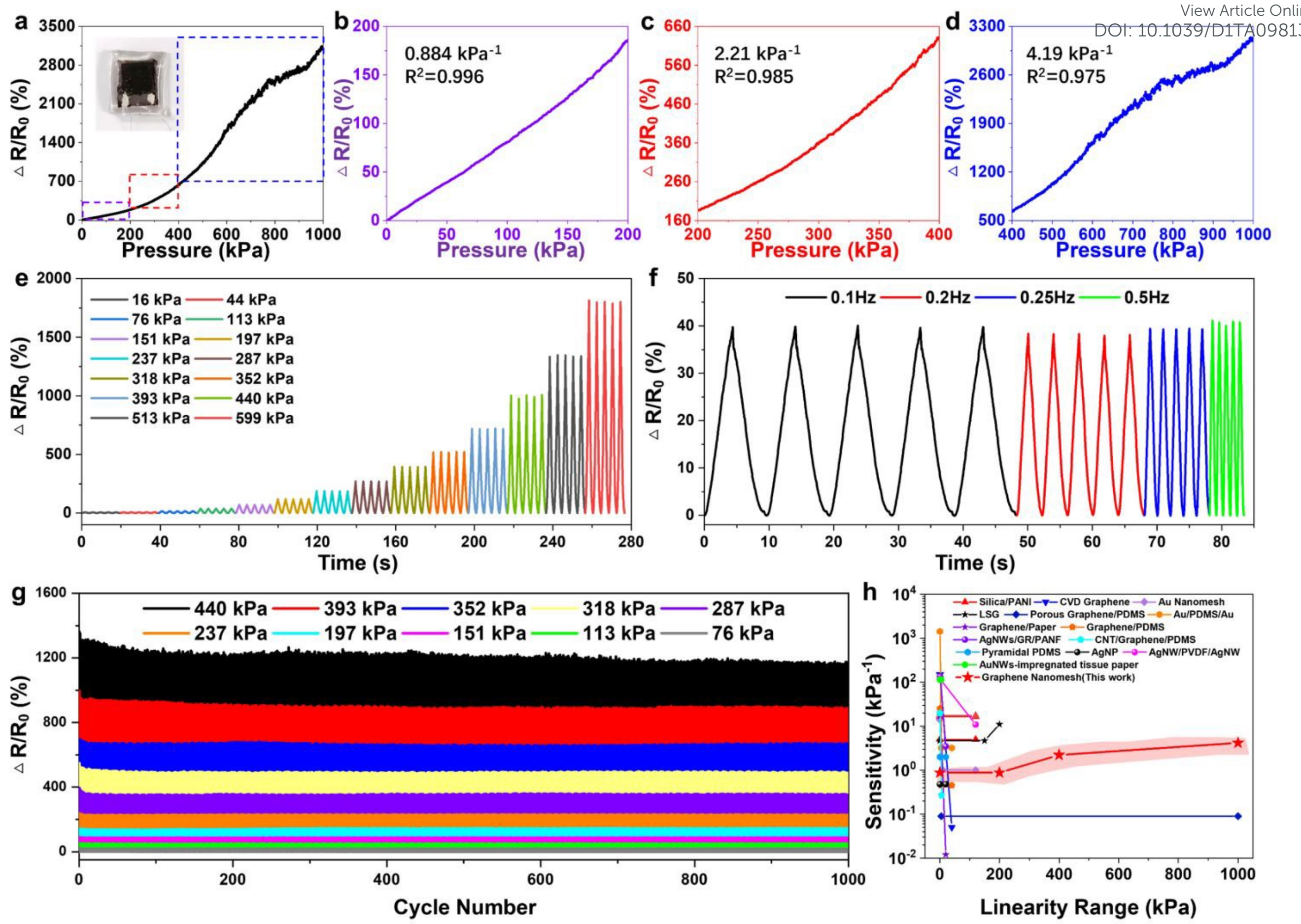

Figure 4. Electromechanical performance of the NRGPSs. (a) Relative resistance variation of NRGPS as the function of the pressure. Inset: the photograph of the NRGPS. (b) Zoom in figure of relative resistance variation of NRGPS in the range of 0 to 200 kPa in the corresponding purple area of Figure 4a. (c) Zoom in figure of relative resistance variation of NRGPS in the range of 200 kPa to 400 kPa in the corresponding red area of Figure 4a. (d) Zoom in figure of relative resistance variation of NRGPS in the range of 400 kPa to 1 MPa in the corresponding blue area of Figure 4a. (e) Relative resistance variation under cyclic compressing/releasing at different pressure (16 kPa, 44 kPa, 76 kPa, 113 kPa, 151 kPa, 197 kPa, 237 kPa, 287 kPa, 318 kPa, 352 kPa, 393 kPa, 440 kPa, 513 kPa, 599 kPa) under the compressing/releasing frequency of 0.25 Hz. (f) Relative resistance variation under cyclic compressing/releasing with the max pressure of 76 kPa at different frequencies of 0.1 Hz, 0.2 Hz, 0.25 Hz, and 0.5 Hz. (g) Relative resistance variation of NRGPS under repeated loading and unloading with different pressure of 76 kPa, 113 kPa, 151 kPa, 197 kPa, 237 kPa, 287 kPa, 318 kPa, 352 kPa, 393 kPa, and 440 kPa for 10000 cycles. The enlarged views of 990 to 1000 cycles are shown in Figure S6. (h) Comparison of the sensitivities and linearity pressure range between the NRGPS and recently published flexible pressure sensor.

Besides, the wet nanomesh-reinforced graphene was transferred onto the skin of the tester. After dried the nanomesh by the commercial hairy drier. During the drying process, the nanomesh-reinforced graphene will be deformed as the skin contour. Therefore, the nanomesh-reinforced graphene can attach the skin firmly with good interface. In addition, the micrometer-level thickness can also lead to the contact interface[42]. By decreasing the PU nanomesh less than 2 μm, the nanomesh-reinforced graphene can still be attached on skin tightly under the tension more than 0.2 N (Figure S6). The tester can carry out their daily life activities, such as drinking water, playing basketball, cutting papers, etc. with nanomesh-reinforced graphene on hand. What's more, the nanomesh-reinforced graphene on hand can be stable when the tester was washing hand (Figure 3b, Movie 1 and 2). The optical coherence tomography (OCT) was used to character the conformal property of the nanomesh-reinforced graphene. The fingerprint of tester was recorded by the OCT (Figure 3c). After covered by the nanomesh-reinforced graphene, the pattern of fingerprint was still clear. The nanomesh on hand after the transfer for 0 h, 3 h, 7 h, and 10 h are illustrated in Figure 3e. The photograph of nanomesh-reinforced graphene on the hand of tester every hour is shown in Figure S7. During the wearing process and after peeling off the nanomesh, the skin has no adverse feeling. Therefore, the nanomesh-reinforced graphene has excellent stability and skin compatibility.

NRGPS

The nanomesh-reinforced graphene can be used as the pressure sensor. Due to the micrometer-level thickness, it is hard to character the electromechanical performance of the nanomesh-reinforced graphene by the universal testing machine. Therefore, the nanomesh-reinforced graphene with the area of 1 cm × 1 cm was packaged by the elastic polydimethylsiloxane (PDMS) to fabricate the pressure sensor. During the application process, the nanomesh-reinforced graphene is transferred to human skin, which can also be regarded as the soft substrate like the PDMS. Besides, the nanomesh-reinforced graphene without any package and the nanomesh-reinforced graphene on non-deformable substrate (polyethylene terephthalate) and covered by PDMS can also be used as the pressure sensor (Figure S8). The linearity range and sensitivity are two important parameters of the pressure sensor. The sensitivity is defined as:

$$S = \frac{\Delta R/R_0}{P} \times 100\% \quad (1)$$

The resistance of traditional negative-resistance pressure sensor become smaller under larger pressure. The max ΔR can only be 100%, which limits the work range of the pressure sensor. On the contrary, the resistance of NRGPS become larger under larger pressure. After 50-cycle pressing and releasing under the pressure of 1 MPa, the NRGPS was tested. Compared with the previous graphene pressure sensor without the nanomesh as the skeleton, the working range of the NRGPS can be up to 1 MPa, which is 5 times than those of the previous work[14]. As shown in the Figure 4a, the NRGPS has three linearity regions (0 - 200 kPa, 200 kPa - 400 kPa, and 400 kPa - 1 MPa). The sensitivity of each region is 0.884 kPa^{-1}, 2.21 kPa^{-1}, and 4.19 kPa^{-1}. In addition, the R^2 of linearity in three regions are 0.996, 0.985, and 0.975, respectively (Figure 4b to 4d). The laser power density is important to the sensitivity. When the power density decreased to 15 mW/cm^2, the sensitivity will be decreased (Figure S9). When the power density increased to 25 mW/cm^2, the laser will destroy the LSG and PU nanomesh. The cyclic pressure of 16 kPa, 44 kPa, 76 kPa, 113 kPa, 151 kPa, 197 kPa, 237 kPa, 287 kPa, 318 kPa, 352 kPa, 393 kPa, 440 kPa, 513 kPa, and 599 kPa were applied to the device (Figure 4e). The resistance response further confirms the resistance variation versus external pressure in Figure 4a. In addition, the NRGPS illustrates the good frequency performance. As shown in Figure 4f, the cyclic 76 kPa pressure at the frequencies of 0.1 Hz, 0.2 Hz, 0.25 Hz, and 0.5 Hz were applied to the pressure sensor. The device has almost the same response independent to the frequency. The NRGPS also displays amazing stability. Each 1000-cycle pressure of 76 kPa, 113 kPa, 151 kPa, 197 kPa, 237 kPa, 287 kPa, 318 kPa, 352 kPa, 393 kPa, and 440 kPa was applied to the NRGPS, and the NRGPS shows stable response (Figure 4g and Figure S10). In other word, the NRGPS can still work well after taken 10000 compressing/releasing cycles under different pressures. Compared with recently published flexible pressure sensor,[7-11, 13, 14, 43-49] NRGPS shows obvious advantage in the linearity range (Figure 4h and Table 1).

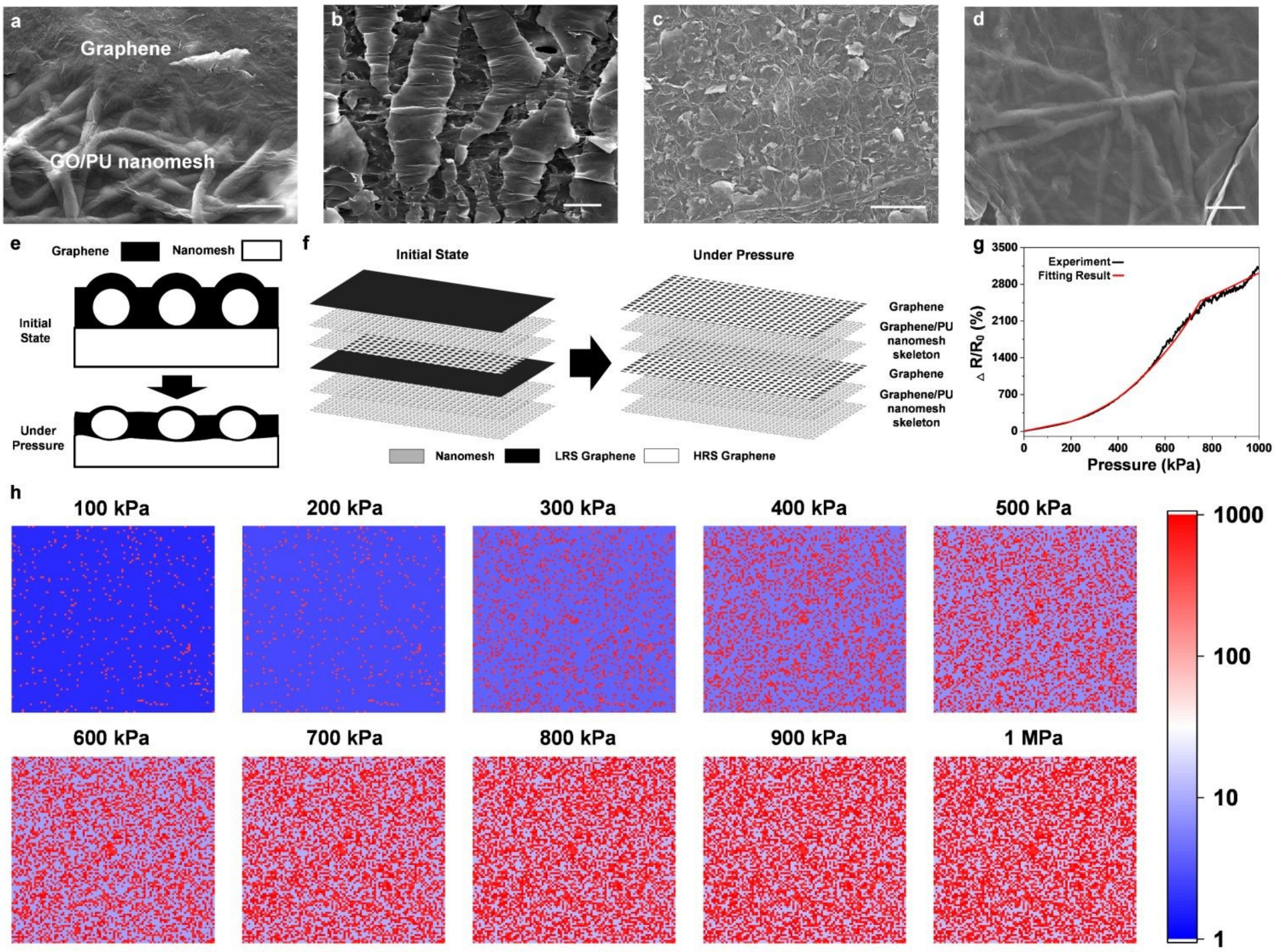

Figure 5. Sensing mechanism and simulation of NRGPSs. (a) The SEM image of the nanomesh embedded into the graphene. The scale bar represents 10 μm. (b) The SEM image of graphene coated on the PU nanomesh after being stretched. The scale bar represents 10 μm. (c) The SEM image of the nanomesh-reinforced graphene after compressing and releasing. The scale bar represents 100 μm. (d) The SEM image of the graphene on the surface of nanomesh. The contour of PU nanomesh is easy to be distinguished. The scale bar represents 5 μm. (e) The diagram of the LSG/PU nanomesh under initial and pressure state. (f) The diagram of nanomesh-reinforced graphene networks under initial and pressure state. High resistance state usually happens at the top of PU nanomesh. (g) Simulation result (red line) and experimental data (black line) of the relative resistance variation of NRGPSs versus the pressure. (h) The resistance distribution results simulated by the finite element model under the pressure from 100 kPa to 1 MPa. The numbers in the label represent the resistance corresponding to the original resistance, which was set to a unit.

View Article Online
DOI: 10.1039/D1TA09813F

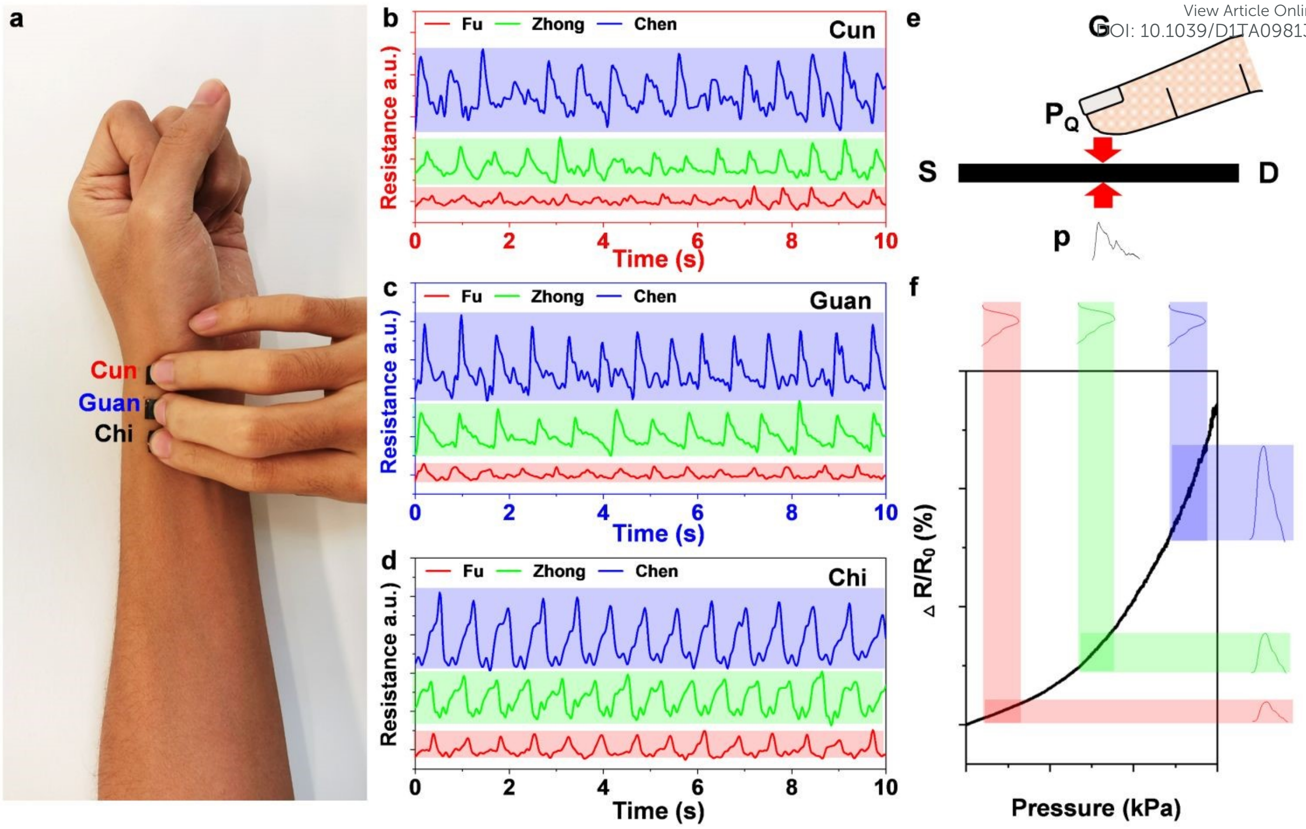

Figure 6. MOSFET-mimicking NRGPS to detect pulse. (a) The photograph of taking the pulse diagnosis. (b) The pulse signals detected by the NRGPS under different pressure at "Cun" acupoint. (c) The pulse signals detected by the NRGPS under different pressure at "Guan" acupoint. (d) The pulse signals detected by the NRGPS under different pressure at "Chi" acupoint. Red signals correspond to pulse under small pressure by finger compressing. Red signals correspond to pulse under middle pressure by finger compressing. Blue signals correspond to pulse under large pressure by finger compressing. (e) Schematic diagram of MOSFET-mimicking NRGPS. The resistance between drain and source is controlled by the mechanical base. (f) The principle of pulse signal amplification by NRGPS. By changing the quiescent point, the magnification can be adjusted.

Sensing Mechanism and Simulation of NRGPS

The large linearity of NRGPS can be attributed to the reinforced concrete structure, which consists of concrete and steel bars. Due to the steel bar skeleton, compared with the concrete, the compressing strength of reinforced concrete can be improved for many times. In addition, the steel bar in reinforced concrete would limit the crack generation and propagation in concrete.

To explain the excellent sensing performance of the NRGPS, the SEM of nanomesh-reinforced graphene was firstly analyzed. The interface between graphene and GO/PU nanomesh was shown in Figure 5a. It is clearly that PU nanomesh was embedded into the graphene similar to the porous reinforced concrete. After stretching the nanomesh-reinforced graphene, the superficial graphene cracked, and the graphene covered and coated on the PU nanomesh tightly can be found (Figure 5b). Compared with the original LSG shown in Figure 1e, after the compressing, the holes in the LSG reduced. Therefore, the effective thickness of NRGPS would reduce. Figure 5c demonstrates the morphology of the LSG on the nanomesh. Compared with the Figure 5a, the contour of PU nanomesh becomes clear (Figure 5d). The surface topography of compressed nanomesh-reinforced graphene was also charactered by the profiler and confocal microscope. After compressed for 30 s under 1 MPa pressure and released (If the compression time is too long, the nanomesh-reinforced graphene would be hard to be peeled off from PDMS for measurement), the thickness of nanomesh-reinforced graphene becomes 22 μm with the STD of 4.03 μm (Figure S11). The fluctuation of nanomesh-reinforced graphene is less than 20 μm (Figure S12 and S13). Therefore, the compression would lead to a flatter surface and smaller height of nanomesh-reinforced graphene. Besides, the LSG on the top of PU nanomesh is first compressed, and easier to become high resistance state (HRS). In addition, some cracks are formed during the pressing process, which also become the HRS. According to the micromorphology of the LSG, a finite element model has been demonstrated to explain the mechanism of the NRGPS. Due to the uneven surface, the contact area between the NRGPS and the pressure probe gradually increased during the compression process, and the density of HRS units gradually increased. The thickness of LSG will be smaller, especially on the top of PU nanomesh (Figure 5e). Therefore, the resistance of normal LSG was usually in low resistance state (LRS), which was set as R_{LRS}. On the contrary, under the pressure, the resistance of LSG on the top of PU nanomesh was in HRS. In addition, cracks are easy to be created at the large-fluctuation area. These units were set as R_{HRS}. The HRS units was formed gradually. The shape of high resistance state area is similar to the PU nanomesh (Figure 5f). The details of the finite element model are discussed in the Finite element model of NRGPS part. As shown in Figure 5g, the simulated result can fit the experimental data well. According to the finite element analyzing result, the resistance distribution of the NRGPS under 100 kPa to 1 MPa pressure are illustrated to in Figure 5h.

Application of Intelligent NRGPS

Based on the high sensitivity and large range, tactile signal such as pulse can be detected by the NRGPS attached on the wrist of tester (radial artery). In addition, the pulse diagnosis for traditional Chinese medicine (TCM) was illustrated. During the common pulse diagnosis, three different pressures (small force call 'Fu' (0.6 N), middle force called 'Zhong' (2 N), large force called 'Chen' (3.6 N)) are usually applied to three acupoints on the radial artery ('Cun', 'Guan', 'Chi') by fingers, and response is detected by the tactile sensation of finger. According to the 9 kinds of response, experienced experts can diagnose the physical condition of the testers by tactile sensation. Therefore, three different pressures were applied on three NRGPSs attached on three acupoints by finger (Figure 6a). It is worth mentioning that the NRGPS would not influence the tactile sensation of the operator, which is important to the data calibration. After filtering, three kinds of pulse signal under different pressure bias at three acupoints were shown in the Figure 6b to 6d. Red, green, and blue signals correspond to pulse under small, middle, and large pressure created by finger. The amplitude of pulse signal was larger under larger pressure. Therefore, the tactile signal was amplified in situ, and the pulse diagnosis process of TCM was realized by the NRGPS, successfully. Similar detection can also be realized in high-pressure condition. The NRGPS was put under the table leg. Then, a mortar less than 100 g was put onto the table, and the signal can be obtained (Figure S14 to S16).

To explain the tactile amplification phenomenon, an analogy between the MOSFET and NRGPS was proposed. The MOSFET consists of gate (G), source (S), and drain (D) (Figure S17a). The drain current can be controlled by the gate voltage. To realize the signal amplification, the MOSFET should be set at appropriate quiescent point (Q) by suitable direct-current (DC) bias. The alternating signal (u_{gs}) was loaded the DC base (U_{GSQ}). Then the u_{gs} will be amplified at the D terminal, and the i_{ds} was controlled by u_{gs} (Figure S17b). Similarly, the resistance between two terminals of NRGPS can also be controlled by pressure terminal. The pressure created by the finger (P_Q) can be regarded as the DC bias. The pulse signals can be regarded as the alternating signal loaded on the P_Q (Figure 6e). By adjusting the P_Q, the pulse can be amplified in situ and the magnification can be controlled (Figure 6f). More details can be obtained under large pressure bias. In addition, the large linearity range and high sensitivity of pressure sensor can enlarge the amplify range. More importantly, traditional negative-resistance pressure sensor, which has the larger sensitivity under small pressure and smaller sensitivity under large pressure, cannot realize signal amplification. Also, the max ΔR of negative-resistance pressure sensor can only be 100%, which leads to the small amplify range when used as the mechanical MOSFET.
Besides, the NRGPS can be applied as the tactile sensor to realize the function of skin, which can help the blind person to learn braille or reconstruct tactile sensation. The braille distinguishing has high

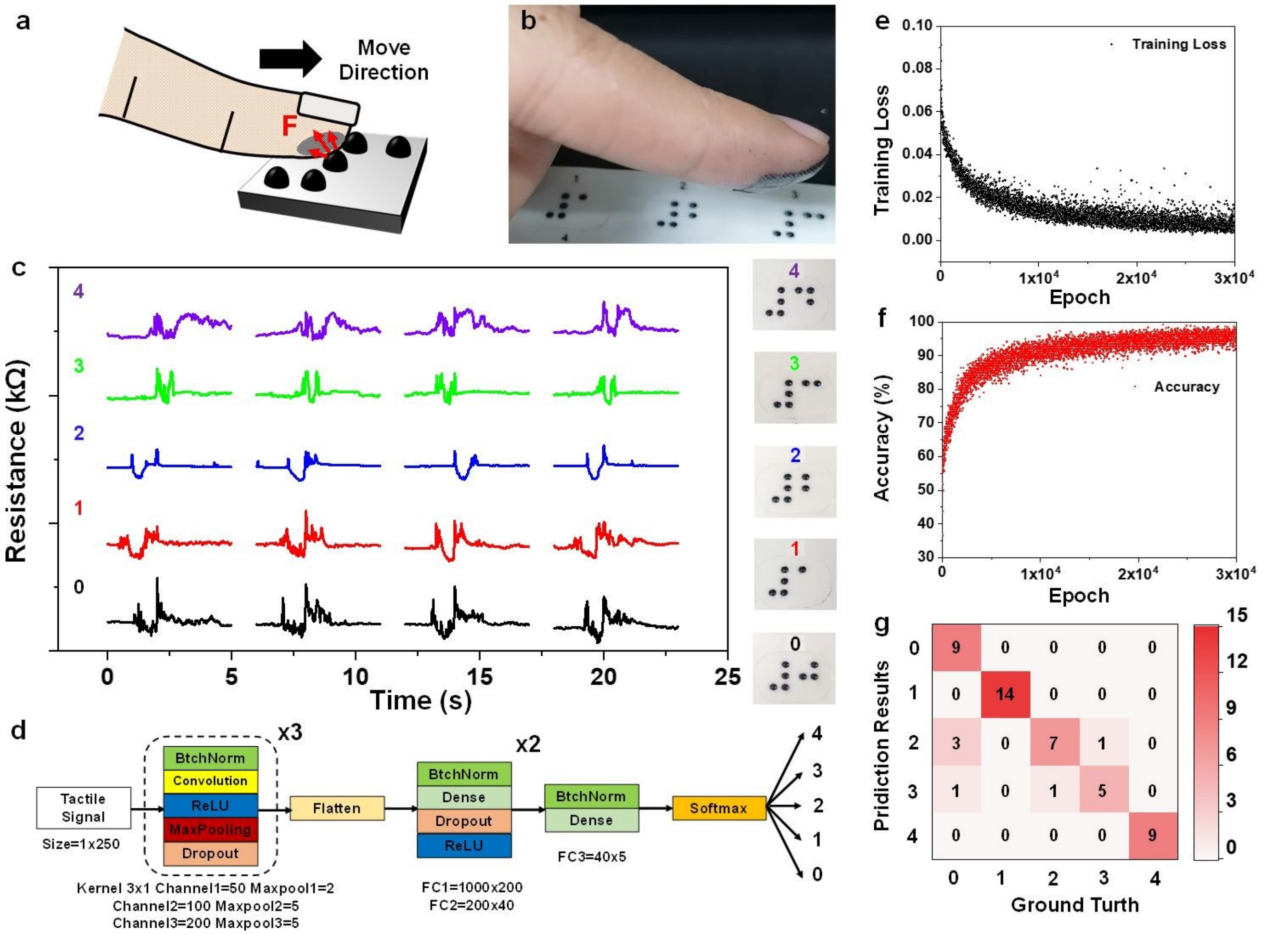

Figure 7. NRGPS as intelligent tactile sensor for distinguishing convex braille numbers. (a) The diagram of touching convex braille number process and pressure condition. (b) Photograph of NRGPS on a finger to press the convex braille number. (c) Tactile signals detected by NRGPS attached on the finger of tester. The tester compressed the convex braille number (0, 1, 2, 3, and 4) by the NRGPS attached on the finger. (d) The structure of CNN to classify the tactile signals. (e) The evolution condition of training loss during 30000 epochs. (f) The evolution condition of classify accuracy during 30000 epochs. (g) The confusion matrix for the CNN prediction result.

View Article Online
DOI: 10.1039/D1TA09813F

requirement to the tactile sensor, especially in the pressure range. The area of a single raised braille is about 1×10^{-6} m^2. If 1 N force was applied to compress the braille, the pressure would be about 1 MPa, which exceeds the range of most flexible sensors. In this work, one piece of nanomesh-reinforced graphene was attached on the finger of tester (Figure 7a and 7b). The arrow represents the moving direction of the finger. Then the tester compressed five convex braille numbers (0, 1, 2, 3, and 4) by the finger with NRGPS on it. The typical tactile signals of different number are illustrated in Figure 7c, which can be distinguished by waveforms. In addition, the photograph of convex braille's practicality picture is also shown in Figure 7c. To realize the information mining and automatic classification, a CNN algorithm was proposed to cooperate with NRGPS, which contains three 1D convolutional layers and three fully connected layers (Figure 7d). The kernel size of three convolutional layers is 1×3, and the channel number of each layer is 50, 100, and 200, respectively. The maxpooling size of each convolutional layer is 2, 5, and 5, successively. The size of three fully connected layer is 1000×200, 200 × 40, and 40 × 5. To avoid gradient explosion and gradient disappearance, ReLU (Rectified Linear Unit) was chosen as the activation function behind each layer. In addition, to solve the overfitting problem, dropout was applied. Finally, the classification results were outputted after the Softmax function. Compared with the previous intelligent tactile sensor, which classify objects by 2D CNN (ResNet-18),[27] the network size and computational load of this 1D CNN is much smaller. Therefore, this 1D CNN is a more efficient algorithm. The tactile signals were first sliced into 5 s fragment according to pressure peaks. Then, tactile signals were inputted into the neural network. After trained for 30000 epochs, the training loss decreased (Figure 7e) and training accuracy can be up to 98.4% (Figure 7f), which shows the optimization of the CNN. The trained CNN can be used to classify the data in the test set. The accuracy of CNN to classify the test set can be up to 88%, and the confusion matrix of classify result is shown in Figure 7g. The result shows that there are hidden characters in the tactile signals of different numbers which can be mined by CNN. In addition, the high classify accuracy of training set is not overfitting, but really good performance. Compared with previous pressure array,[27] the automatically tactile classification has been realized by only one NRGPS, which greatly decreases the cost of the sensor. In all, based on the excellent sensing performance, the NRGPS can monitor physiological signals internally and reconstruct the tactile function of skin externally.

Experimental

Fabrication of Packaged NRGPS

The PU nanomesh was fabricated using a electrospinning machine (Ucalery). The experimental details has been introduced in the main text. To character the performance of NRGPS, the nanomesh-reinforced graphene was packaged by the PDMS (SYLGARD 184, Dow Corning, 10:1 mixture). The liquid PDMS was cured under 70 ℃ for 3 h as the substrate. Then, nanomesh-reinforced graphene (1 cm× 1 cm) was transferred to the PDMS substrate. The Cu wires as the electrode were fixed on the nanomesh-reinforced graphene by Ag gel. Then the Ag gel was cured under a baking lamp for 12 h. Finally, another layer of uncured PDMS liquid was poured on the nanomesh-reinforced graphene. The top PDMS layer was cured by put the device on the hot plated under 70 ℃ for 3 h.

Characterization

The surface morphology of the LSG was observed using a JCM-7000 SEM (JEOL Inc.) and confocal microscope (Leica DCM8). The thickness of the PU nanomesh and LSG were measured using the profilers (Dektak 150). Raman spectroscopy was performed using a laser with a wavelength of 532 nm (HORIBA Inc.). The XPS (PHI Quantro SXM) was performed using monochromatic aluminum Kα X-rays. The loadings of pressure were performed with a universal testing machine (Shimadzu AGS-X). The electrical signals of the pressure sensor were recorded using a digital source-meter (RIGOL DM 3068 and Keithley DMM6500). The power density of the laser was measured using an optical power meter (THORLABS S130C). The pattern of fingerprint was measured using an OCT (HSO-2000, TEKSQRAY).

Finite element model of NRGPS

The NRGPS was divided into 100×100 units, which starts from the Ohm's law (equation (2)), where ρ is the resistivity of the whole networks. S, H, L, and W are the cross-sectional area, effective thickness, length, and width of the unit, respectively. The L and W of the unit is equal. The original R_{LRS} is set to 1. With the increasing of pressure, the H will be smaller.

$$R = \rho\frac{L}{S} = \rho\frac{L}{WH} = \frac{\rho}{H} \quad (2)$$

Similar to the steel bar in reinforced concrete, the PU nanomesh is important to the performance of pressure sensor. As Wu et. al. recently published graphene pressure sensor without the PU nanomesh, the graphene pressure sensor has the linearity range of 200 kPa[14]. However, when the compressing pressure larger than 200 kPa, the graphene pressure sensor would be in an unstable state. The PU nanomesh play the role of the skeleton to the LSG and greatly improve the linearity range of pressure sensor. In the pressure range of 0 to 200 kPa, due to the exist of PU nanomesh, the density of units in HRS changes slowly. The generation rate of units in HRS is set to 2 unit/kPa. The positions of HRS unit are random. The resistance of newly formed R_{HRS} is 400. In addition, the H also decreases slowly and microcracks in LRS unit make the R_{LRS} increase as the equation (3), the unit of P is kPa.

$$R_{LRS} = 1 + \frac{P}{155} \quad (3)$$

In the pressure range of 200 kPa to 400 kPa, the thickness LSG on the top of PU nanomesh changes quickly. Therefore, the HRS units changes fast. The generation rate of units in HRS increases to 12.5 unit/kPa. The resistance of newly formed R_{HRS} is 600. In addition, the R_{LRS} increases as the equation (4), the unit of P is kPa.

$$R_{LRS} = 2.74 + \frac{(P - 200)}{80} \quad (4)$$

When 400 kPa<P<750 kPa, the density of HRS units caused by the LSG on the top of PU nanomesh changes slower. However, the recoverable cracks are also created due to the high pressure, which also makes HRS units. The generation rate of units in HRS decreases to 6.9 unit/kPa in average. The resistance of newly formed R_{HRS} is 1000. The high pressure also decreases the thickness of LSG in the LRS unit. The high pressure creates much microcrack in LRS units, which makes the resistance of LRS units increase fast. the R_{LRS} increases as the equation (5), the unit of P is kPa.

$$R_{LRS} = 5.24 + \frac{(P - 400)}{50} \quad (5)$$

When 750 kPa<P<1 MPa, the thickness and crack number of NRGPS are tend to be saturated. The generation rate of units in HRS decreases to 1.2 unit/kPa in average. The resistance of newly formed R_{HRS} is also 1000. In addition, the R_{LRS} increases much slowly as the equation (6), the unit of P is kPa.

$$R_{LRS} = 12.24 + \frac{(P - 750)}{150} \quad (6)$$

View Article Online
DOI: 10.1039/D1TA09817F

Details of CNN and Tactile Signal

The sampling rate of tactile signal is 50 Hz. The continuing tactile signals were first sliced into fragments according to the peaks of each compressing. Each fragment has 5s signal (250 data points). Therefore, the size of input of the CNN is 1×250. 303 fragments were randomly divided into 253 training set and 50 test set. The batch size is set to 16. Normalized tactile fragments were first inputted into the three sequential 1D CNN layers. Afterthat, the flatten data was transferred to three fully connected layers. Finally, CrossEntropy was chosen as the loss function. Adam was chosen as the opitmizer. The learning rate was 0.00005 from 1 to 50 epochs, 0.00001 from 51 to 500 epochs, and 0.000005 from 501 to 30000 epochs. Details of each nerual network layer is listed below:

CNN layer1: kernel size = 1 × 3, padding = 1, stride = 1, activation function = ReLU, maxpooling size = 2, channel number = 50, dropout = 0.5;

CNN layer2: kernel size = 1 × 3, padding = 1, stride = 1, activation function = ReLU, maxpooling size = 5, channel number = 100, dropout = 0.5;

CNN layer3: kernel size = 1 × 3, padding = 1, stride = 1, activation function = ReLU, maxpooling size = 5, channel number = 200, dropout = 0.5;

Fully connected layer1: size = 1000×200, activation function = ReLU, dropout = 0.5;

Fully connected layer2: size = 200 × 40, activation function = ReLU, dropout = 0.5;

Fully connected layer3: size = 40 × 5, activation function = ReLU, dropout = 0.5;

Conclusions

Table 1. Comparison of the sensitivities and linearity pressure range among the NRGPS and recently published flexible pressure sensor.

Material	Fixing Method	Breathable on Body	Intelligent	Linearity Range	Sensitivity at Max Range	Reference
Nanomesh-reinforced graphene	**Self-Fixation**	**Yes**	**Yes**	**1000**	**4.19**	**This work**
Graphene/Paper	Tape	Yes, if not packaged	No	20	0.012	[7]
Graphene/PDMS	Tape	No	No	40	0.45	[8]
CNT/Graphene/PDMS	N.A.	No	No	5.8	0.27	[9]
AgNWs/GR/PANF	Tape	Yes, if not packaged	No	80	0.7	[10]
AuNWs-impregnated tissue paper	Tape	No	No	5	1.14	[11]
Au Nanomesh	Self-Fixation	Yes	No	120	1	[13]
LSG	Bandage	No	No	200	11.09	[14]
Silica/PANI	Bandage	No	No	120	17.5	[34]
CVD Graphene	N.A.	No	No	40	0.00005	[37]
Porous Graphene/PDMS	Bandage and Tape	No	No	1000	0.09	[38]
Au/PDMS/Au	Tape	No	No	40	3.2	[40]
Pyramidal PDMS	N.A.	No	No	600	0.021	[41]
AgNPs	Bandage and Tape	No	No	20	0.48	[43]
AgNWs/PVDF/AgNWs	Bandage and Tape	No	Hardware Circuit	120	10.9	[44]

In conclusion, the intelligent NRGPS was realized based on the materials of PU nanomesh, LSG and the fabriction process with a high-effiencecy and low-cost. The as-prepared nanomesh-reinforced graphene exhibits good water vapor permeability like no obstruction. With the nanomesh skeleton, the NRGPS has the ultra-large linearity (1 MPa), high sensitivity (4.19 kPa^{-1}), and excellent mechanical stablity (10000 compressing/releasing cycles), which shows advantage to recently published work. The intelligent NRGPS can amplify the pulse signal in situ to realize the pulse diagnosis of traditional Chinese medicine. Combined with the CNN algorithm, the intelligent NRGPS can also be used as tactile sensor to distinguish the braille numbers. This work has great potential in the intelligent diagnosis field, human–computer interaction, and helping disables to reconstruct tactile sensation.

Author Contributions

Y Qiao, J Jian, H Tang, S Ji, Y Liu, H Liu, T Cui, and G Gou carried out the experiments. Y Li, F Han, Z Liu, L Jiang, and Y Yang gave the equipment support and help the experiments. Y Qiao and X Li designed the CNN algorithm. Y Qiao, T Ren, and J Zhou conceived the project, designed, and supervised the research. Y Qiao, J Jian, B Zhou, T Ren, and J Zhou wrote and revised the article.

Conflicts of interest

There are no conflicts to declare.

Acknowledgements

This work was supported by the Guangdong Basic and Applied Basic Research Foundation (2019A1515111183), National Natural Science Foundation of China (No. 32000939; 21775168; 22174167; 51861145202; U20A20168), Shenzhen Research Funding Program (JCYJ20190807160401657; JCYJ201908073000608; JCYJ20150831192224146), the National Key R&D Program (2018YFC2001202). The authors are also thankful for the support of the Research Fund from Tsinghua University Initiative Scientific Research Program the support from Key Laboratory of Sensing Technology and Biomedical Instruments of Guangdong Province (No. 2020B1212060077).

Notes and references

1 L. Pan, A. Chortos, G. Yu, Y. Wang, S. Isaacson, R. Allen, Y. Shi, R. Dauskardt and Z. Bao, Nat. Commun., 2014, **5**, 1-8.
2 D. Chen and Q. Pei, Chem. Rev., 2017, **117**, 11239-11268.
3 T. R. Ray, J. Choi, A. J. Bandodkar, S. Krishnan, P. Gutruf, L. Tian, R. Ghaffari and J. A. Rogers, Chem. Rev., 2019, **119**, 5461-5533.
4 C. M. Boutry, Y. Kaizawa, B. C. Schroeder, A. Chortos, A. Legrand, Z. Wang, J. Chang, P. Fox and Z. Bao, Nat. Electron., 2018, **1**, 314-321.
5 C. M. Boutry, A. Nguyen, Q. O. Lawal, A. Chortos, S. Rondeau - Gagné and Z. Bao, Adv. Mater, 2015, **27**, 6954-6961.
6 Y. Chu, J. Zhong, H. Liu, Y. Ma, N. Liu, Y. Song, J. Liang, Z. Shao, Y. Sun and Y. Dong, Adv. Funct. Mater., 2018, **28**, 1803413.
7 L.-Q. Tao, K.-N. Zhang, H. Tian, Y. Liu, D.-Y. Wang, Y.-Q. Chen, Y. Yang and T.-L. Ren, ACS Nano, 2017, **11**, 8790-8795.
8 Y. Pang, K. Zhang, Z. Yang, S. Jiang, Z. Ju, Y. Li, X. Wang, D. Wang, M. Jian and Y. Zhang, ACS Nano, 2018, **12**, 2346-2354.
9 M. Jian, K. Xia, Q. Wang, Z. Yin, H. Wang, C. Wang, H. Xie, M. Zhang and Y. Zhang, Adv. Funct. Mater., 2017, **27**, 1606066.
10 X. Li, Y. J. Fan, H. Y. Li, J. W. Cao, Y. C. Xiao, Y. Wang, F. Liang, H. L. Wang, Y. Jiang and Z. L. Wang, ACS Nano, 2020, **14**, 9605-9612.
11 S. Gong, W. Schwalb, Y. Wang, Y. Chen, Y. Tang, J. Si, B. Shirinzadeh and W. Cheng, Nat. Commun., 2014, **5**, 1-8.
12 Y. Ko, J. Kim, D. Kim, Y. Yamauchi, J. H. Kim and J. You, Sci. Rep., 2017, **7**, 2282.
13 S. Lee, S. Franklin, F. A. Hassani, T. Yokota, M. O. G. Nayeem, Y. Wang, R. Leib, G. Cheng, D. W. Franklin and T. Someya, Science, 2020, **370**, 966-970.
14 Q. Wu, Y. Qiao, R. Guo, S. Naveed, T. Hirtz, X. Li, Y. Fu, Y. Wei, G. Deng and Y. Yang, ACS Nano, 2020, **14**, 10104-10114.
15 Y. J. Park, B. K. Sharma, S. M. Shinde, M.-S. Kim, B. Jang, J.-H. Kim and J.-H. Ahn, ACS Nano, 2019, **13**, 3023-3030.
16 Y.-W. Cai, X.-N. Zhang, G.-G. Wang, G.-Z. Li, D.-Q. Zhao, N. Sun, F. Li, H.-Y. Zhang, J.-C. Han and Y. Yang, Nano Energy, 2021, **81**, 105663.
17 I. You, S. E. Choi, H. Hwang, S. W. Han, J. W. Kim and U. Jeong, Adv. Funct. Mater., 2018, **28**, 1801858.
18 Y. Qiao, Y. Wang, H. Tian, M. Li, J. Jian, Y. Wei, Y. Tian, D.-Y. Wang, Y. Pang, X. Geng, X. Wang, Y. Zhao, H. Wang, N. Deng, M. Jian, Y. Zhang, R. Liang, Y. Yang and T.-L. Ren, ACS Nano, 2018, **12**, 8839-8846.
19 Y. Wan, Z. Qiu, Y. Hong, Y. Wang, J. Zhang, Q. Liu, Z. Wu and C. F. Guo, Adv. Electron. Mater., 2018, **4**, 1700586.
20 H. Niu, S. Gao, W. Yue, Y. Li, W. Zhou and H. Liu, Small, 2020, **16**, 1904774.
21 D. Choi, S. Jang, J. S. Kim, H. J. Kim, D. H. Kim and J. Y. Kwon, Adv. Mater. Technol., 2019, **4**, 1800284.
22 Z. Liang, J. Cheng, Q. Zhao, X. Zhao, Z. Han, Y. Chen, Y. Ma and X. Feng, Adv. Mater. Technol., 2019, **4**, 1900317.
23 C. Wu, T. W. Kim, J. H. Park, B. Koo, S. Sung, J. Shao, C. Zhang and Z. L. Wang, ACS Nano, 2019, **14**, 1390-1398.
24 J. Yu, X. Hou, M. Cui, S. Zhang, J. He, W. Geng, J. Mu and X. Chou, Nano Energy, 2019, **64**, 103923.
25 X. Wang, Y. Zhang, X. Zhang, Z. Huo, X. Li, M. Que, Z. Peng, H. Wang and C. Pan, Adv. Mater., 2018, **30**, 1706738.
26 Y. Wu, Y. Liu, Y. Zhou, Q. Man, C. Hu, W. Asghar, F. Li, Z. Yu, J. Shang and G. Liu, Sci. Robot., 2018, **3**.
27 P. Zhu, Y. Wang, Y. Wang, H. Mao, Q. Zhang and Y. Deng, Adv. Energy Mater., 2020, **10**, 2001945.
28 W. Lin, B. Wang, G. Peng, Y. Shan, H. Hu and Z. Yang, Adv. Sci., 2021, **8**, 2002817.
29 S. Sundaram, P. Kellnhofer, Y. Li, J.-Y. Zhu, A. Torralba and W. Matusik, Nature, 2019, **569**, 698-702.
30 H.-J. Lin and C.-I. Liao, Compos. Struct., 2004, **65**, 239-250.
31 F. Moccia, Q. Yu, M. Fernández Ruiz and A. Muttoni, Struct. Concr., 2021, **22**, E634-E654.
32 S. A. Ashour, F. F. Wafa and M. I. Kamal, Eng. Struct., 2000, **22**, 1145-1158.
33 K. L. Chung, L. Yuan, S. Ji, L. Sun, C. Qu and C. Zhang, Appl. Sci., 2017, **7**, 177.
34 A. Shende, A. Pande and M. G. Pathan, Int. Ref. J. Eng. Sci., 2012, **1**, 043-048.
35 J. Choi, P. Wagner, R. Jalili, J. Kim, D. R. MacFarlane, G. G. Wallace and D. L. Officer, Adv。 Energy Mater., 2018, **8**, 1801280.
36 J. Choi, J. Kim, P. Wagner, S. Gambhir, R. Jalili, S. Byun, S. Sayyar, Y. M. Lee, D. R. MacFarlane, G. G. Wallace and D. L. Officer, Energy Environ. Sci., 2019, **12**, 747-755.
37 S. Lee, D. Sasaki, D. Kim, M. Mori, T. Yokota, H. Lee, S. Park,

View Article Online
DOI: 10.1039/D1TA09813F

K. Fukuda, M. Sekino and K. Matsuura, Nat. Nanotechnol., 2019, **14**, 156-160.
38 A. Miyamoto, S. Lee, N. F. Cooray, S. Lee, M. Mori, N. Matsuhisa, H. Jin, L. Yoda, T. Yokota and A. Itoh, Nat. Nanotechnol., 2017, **12**, 907-913.
39 H. Tian, Y. Yang, D. Xie, Y.-L. Cui, W.-T. Mi, Y. Zhang and T.-L. Ren, Sci. Rep., 2014, **4**, 3598.
40 X. Fan, K. Nose, D. Diao and T. Yoshida, Appl. Surf. Sci., 2013, **273**, 816-823.
41 Y. Chyan, R. Ye, Y. Li, S. P. Singh, C. J. Arnusch and J. M. Tour, ACS Nano, 2018, **12**, 2176-2183.
42 J. W. Jeong, W. H. Yeo, A. Akhtar, J. J. Norton, Y. J. Kwack, S. Li, S. Y. Jung, Y. Su, W. Lee and J. Xia, Adv. Mater., 2013, **25**, 6839-6846.
43 Y.-R. Kim, M. P. Kim, J. Park, Y. Lee, S. K. Ghosh, J. Kim, D. Kang and H. Ko, ACS Appl. Mater. Interfaces, 2020, **12**, 58403-58411.
44 X. Song, T. Sun, J. Yang, L. Yu, D. Wei, L. Fang, B. Lu, C. Du and D. Wei, ACS Appl. Mater. Interfaces, 2016, **8**, 16869-16875.
45 Y. Pang, H. Tian, L. Tao, Y. Li, X. Wang, N. Deng, Y. Yang and T.-L. Ren, ACS Appl. Mater. Interfaces, 2016, **8**, 26458-26462.
46 X. Zeng, Z. Wang, H. Zhang, W. Yang, L. Xiang, Z. Zhao, L.-M. Peng and Y. Hu, ACS Appl. Mater. Interfaces, 2019, **11**, 21218-21226.
47 S. R. A. Ruth, L. Beker, H. Tran, V. R. Feig, N. Matsuhisa and Z. Bao, Adv. Funct. Mater., 2020, **30**, 1903100.
48 L. W. Lo, H. Shi, H. Wan, Z. Xu, X. Tan and C. Wang, Adv. Mater. Technol., 2020, **5**, 1900717.
49 Q. Liu, Z. Liu, C. Li, K. Xie, P. Zhu, B. Shao, J. Zhang, J. Yang, J. Zhang and Q. Wang, Adv. Sci., 2020, **7**, 2000348.